




# Scalable Electric-motor-in-the-Loop Testing for Vehicle Powertrains

Thomas D'hondt<sup>1</sup><sup>a</sup>, Yves Mollet<sup>1,2</sup><sup>b</sup>, Arthur Jacques Joos<sup>2</sup>, Leonardo Cecconi<sup>1</sup>,  
Mathieu Sarrazin<sup>1</sup> and Johan Gyselincx<sup>2</sup><sup>c</sup>

<sup>1</sup>Test Division, Siemens Industry Software NV, Researchpark 1237, Interleuvenlaan 68, B-3001 Leuven, Belgium

<sup>2</sup>BEAMS Department, Université Libre de Bruxelles, Avenue Franklin Roosevelt 50, CP165/52, B-1050 Bruxelles, Belgium

**Keywords:** Electric Vehicles, e-Powertrain, Model-Based System Testing, Scaling, Real-time Control, X-in-the-Loop.

**Abstract:** Model-Based System Testing (MBST) combines physical testing and simulation models to enable the validation of complex systems early-on in their design cycle. Therefore, it shows great potential for the validation of increasingly complex Electric Vehicle (EV) powertrains. In this work, the MBST methodology is applied to a downscaled powertrain, including a Permanent-Magnet Synchronous Machine (PMSM) and a 3-phase switch-mode inverter. This System-under-Test (SuT) is integrated into an X-in-the-Loop (XiL) test bench, where real-time simulation models of the rest of the vehicle are used to impose realistic boundary conditions to the SuT. These include the emulation of the vehicle inertia, its friction losses and the regenerative braking controller. Both hardware and software architectures required to achieve this setup are presented. Subsequently, a methodology used for computing scaling factors that match the power levels of the full vehicle to the miniature test bench is proposed. Finally, the combined physical-virtual system is evaluated on a driving cycle to validate its behaviour. The usage of a downscaled SuT constitutes the first step towards full-scale E-powertrain-in-the-loop testing, as well as a valuable multi-purpose didactical XiL setup.


## 1 INTRODUCTION


In Model-Based System Testing (MBST), simulation models and physical testing are combined to investigate, improve or validate complex multi-physical or mechatronic systems (Siemens Digital Industries Software, 2019). In this framework, X-in-the-Loop (XiL) testing is more specifically used to test one or more physical components, while simulating their environment, such that the physical presence of the surrounding hardware is not required to create realistic working conditions (Van der Auweraer et al., 2017). As a consequence, XiL-based prototyping can be performed at early development stages and requires limited hardware compared to its physical counterpart, permitting a shorter time-to-market and lower development costs (Fathy et al., 2006).


This technique is particularly interesting for research and development in Electric Vehicles (EVs), especially focusing on drivetrain (Popp et al., 2015; Petersheim and Brennan, 2009; Yang et al., 2015) and

consumption (Ciceo et al., 2016; Williamson et al., 2006) to address their present shortages in efficiency, autonomy and acoustic comfort, in the challenging context of more and more restrictive ecological and safety regulations (Fiori et al., 2016; Yang et al., 2014). In this domain, XiL testing also allows for high repeatability compared to real driving and may avoid increased computation time or resources in case of full-vehicle simulation (Fathy et al., 2006). This is of paramount interest as more complex powertrains and increasing amounts of electrical accessories can result in integration issues if combined late in the design process. Therefore, the application of the MBST methodology on EVs is currently being studied in the OBELICS (Optimization of scalaBle rEaltime modeLs and functional testing for e-drive Concepts) research project (Obelics consortium, 2019).

A surrogate System-under-Test (SuT) can be used to reduce prototyping costs when the original hardware is not required for the investigations of interest (Petersheim and Brennan, 2009). Adequate scaling factors allow then to match the characteristics of the SuT to the model. This principle is used in the present paper to significantly downscale the surrogate SuT compared to similar setups (Popp et al., 2015;

<sup>a</sup>  <https://orcid.org/0000-0003-2554-332X>

<sup>b</sup>  <https://orcid.org/0000-0001-6170-0148>

<sup>c</sup>  <https://orcid.org/0000-0003-2259-8560>



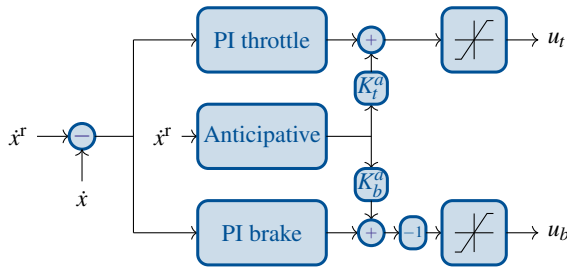


Figure 3: Driver controller layout.

quantities respectively. Similarly, the subscripts  $t$  and  $b$  correspond to the throttle and brake actions. Finally, tilde variables are referred to the reduced-power test bench, whereas regular variables correspond to the full-scale EV.

Two independent Proportional Integral (PI) controllers with an additional anticipative action are used to compute the vehicle inputs (Figure 3). The anticipative action is calculated using an approximated reference acceleration:

$$u^a = \frac{\dot{x}^r(t + \Delta T) - \dot{x}^r(t)}{\Delta T}, \quad (1)$$

where  $\Delta T$  is the anticipative time constant. It is then multiplied by throttle- and brake-specific gains and summed to the outputs of the regular PI controllers. Finally, both the throttle and braking action are saturated in the  $[0, 1]$  interval.

## 2.2 Vehicle Control Unit

The VCU converts the computed throttle and brake commands into a reference torque for the E-motor  $\tau_e^r$  and for the mechanical brakes  $\tau_b$ , taking regenerative braking into account (Figure 1). Therefore, a user-requested torque  $\tau^r$  is first computed by transforming the normalised user inputs into a torque value:

$$\tau^r = u_t \tau_e^{\max} + u_b \left( \tau_e^{\min} - \frac{\tau_b^{\max}}{r} \right), \quad (2)$$

where  $\tau_e^{\max} > 0$  and  $\tau_e^{\min} \leq 0$  are the maximum E-motor torques in motoring and braking operation. The maximum mechanical braking torque  $\tau_b^{\max} > 0$  of the vehicle is referred to the shaft of the E-motor by dividing it by the gearbox ratio  $r$ . The user-requested torque  $\tau^r$  is then split according to a fixed repartition strategy (Figure 4). The blue and green areas represent the contribution of  $\tau_e^r$  and  $\tau_b$  to the total vehicle torque referred to the E-motor shaft. During the braking operation, the fixed ratio is held until  $\tau_e^r$  reaches the braking torque limit of the E-motor  $\tau_e^{\min}$ . Although not further studied in this paper, the regenerative action can also be inhibited at too low or too high speeds and depending on battery state-of-charge.

## 2.3 Vehicle Dynamics

The vehicle body is simulated as a point-mass moving in the longitudinal dimension  $x$ . The equivalent mass of the vehicle includes both the vehicle mass  $M$  and its wheel inertia  $J_w$ :

$$\left( M + 4 \frac{J_w}{R_w^2} \right) \ddot{x} = \frac{r \tau_e^m - \tau_b}{R_w} - F_r, \quad (3)$$

with  $R_w$ ,  $\tau_e^m$  and  $\tau_b$  the wheel radius, the measured and upscaled E-motor torque and the braking torque. Both torques are transformed into longitudinal forces considering the fixed and unitless reducer gear ratio  $r$  and the wheel radius  $R_w$ . Finally, the resistive force exerted by the environment on the car  $F_r$  comprises both aerodynamic drag and rolling resistance:

$$F_r = \frac{\rho_{\text{air}} C_x S}{2} \dot{x}^2 + Mg(a + b\dot{x}), \quad (4)$$

with  $\rho_{\text{air}}$  the air density,  $C_x$  the air penetration coefficient and  $S$  the vehicle active area. No external wind is currently considered in the aerodynamic drag term. The rolling resistance is supposed to be proportional to the vehicle mass  $M$  and the gravity  $g$  with a constant term  $a$  and a term proportional to the vehicle speed  $b\dot{x}$ . It should be noted that no slope, nor stiction effects are considered in the present paper.

A friction torque compensation mechanism is included in the simulation model due to the non-negligible friction in the test setup compared to the nominal torque of the machines. Indeed, the electromagnetic torque  $\tilde{\tau}_l^m$  estimated by the load inverter based on current measurements differs from the electromagnetic torque  $\tilde{\tau}_e^m$  from the SuT motor expected by the vehicle simulation model. The difference between both corresponds to the friction of the loading

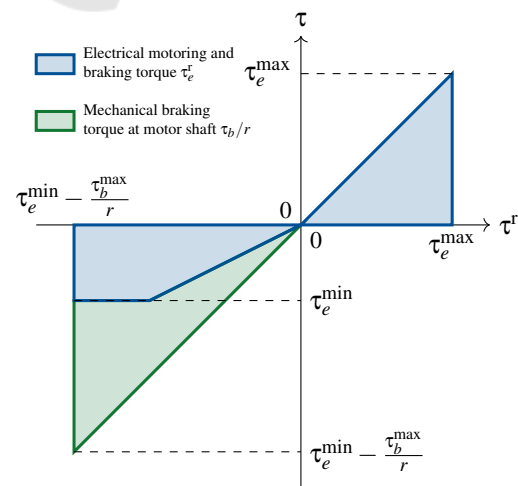


Figure 4: Split between regenerative and mechanical torques during braking manoeuvres.

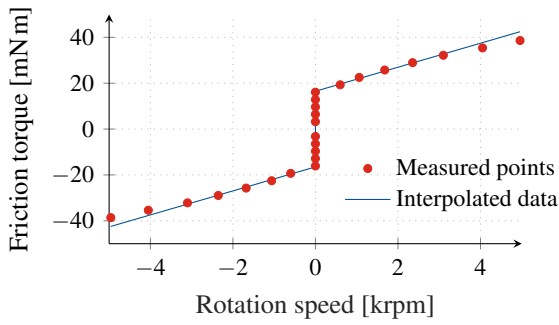


Figure 5: Test bench friction  $\tilde{\tau}_f$  as a function of rotational speed  $\tilde{\omega}^m$ .

machine  $\tilde{\tau}_e^m = \tilde{\tau}_l^m + \tilde{\tau}_f$ , which is identified during preliminary tests at constant speed and approximated using a first-order relation:

$$\tilde{\tau}_f(\tilde{\omega}^m) = \text{sign}(\tilde{\omega}^m) (\tau_{f,0} + K_f |\tilde{\omega}^m|), \quad (5)$$

where  $\tau_{f,0}$  and  $K_f$  are the static and dynamic friction coefficients. The measured and interpolated data used in the simulation model are represented in Figure 5.

### 3 CONSTRUCTION OF THE XiL TEST BENCH

The downscaled XiL test setup created for this work consists of three main subsystems: (i) the power cabinet, (ii) the real-time computing unit and (iii) the E-motor testbed. All three are visible in Figure 6.

The power cabinet and the testbed contain two motor and inverter pairs: the powertrain-under-test

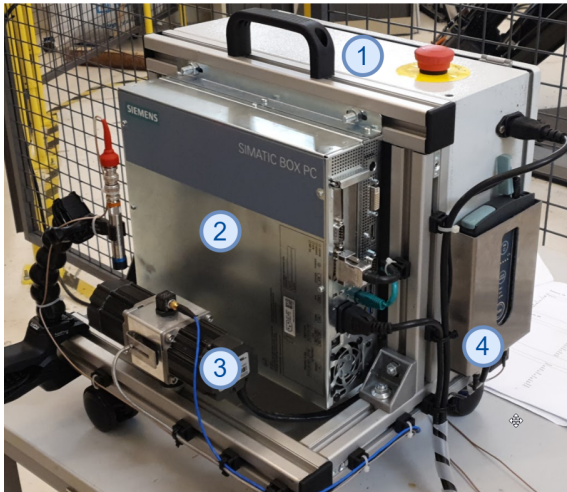


Figure 6: The power supply and inverters are located inside the electrical power cabinet (1). The real-time controller (2) is fixed on a frame, which also supports the electric motors using a small vibration absorber (3). A DAQ is mounted on the side of the setup (4).

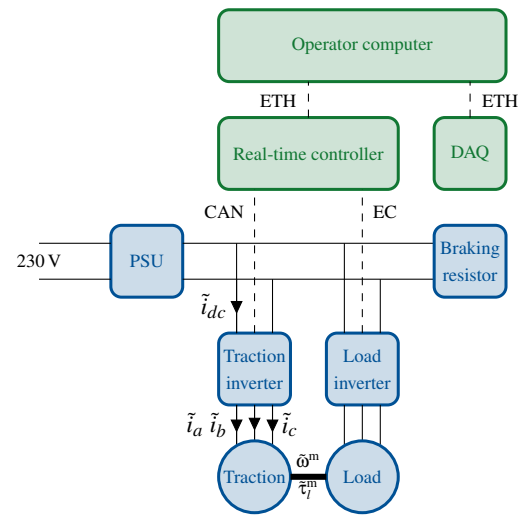


Figure 7: Electrical scheme of the test setup.

and its load (Figure 7). Both traction and load motors use the same low-power PMSM, whose specifications are provided in Tables 1 and 2. Their rotor shafts are connected through a spider coupling, while their stators are rigidly mounted and aligned with a metallic bracket.

The traction motor is controlled by a Texas Instruments (TI) inverter development kit, whose torque control algorithms can be freely tuned by the test engineer (Texas Instruments, 2017). Its controller chip is similar to the ones used in commercial road car powertrain applications; only the power levels are reduced. The load motor is controlled by a maxon EPOS 3 industrial inverter, which operates in speed-controlled mode. Finally, a 37.3 V DC-bus is provided by a regular industrial Power Supply Unit (PSU), which is protected from over-voltage during sudden braking manoeuvres by a braking resistor and a chopper. Both inverters share their DC-bus to enable the recirculation of the generated power.

The test bench is controlled from a real-time computing unit whose objectives are twofold: (i) execute the above detailed real-time simulation model of the vehicle and of the driver and (ii) handle the communication between the simulation model and the phys-

Table 1: Specifications of the PMSM used on the testbed.

Parameter	Symb.	Value
Pole pairs	$p$	4
Voltage constant	$K_e$	4.75 V <sub>ph-ph</sub> /krpm
Torque constant	$K_t$	0.04533 N m/A
Stator resistance	$R_s$	0.36 Ω (25° C)
d-axis inductance	$L_d$	0.201 mH
q-axis inductance	$L_q$	0.201 mH
Rotor inertia	$J_r$	7 kg mm <sup>2</sup>



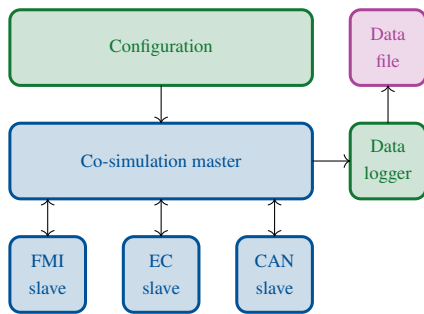


Figure 8: Structure of the real-time controller. Blue, green and purple blocks correspond to hard real-time processes, non-real-time processes and output files respectively.

ical components on the testbed (Figure 7). As in a real automotive use case, the torque  $\tilde{\tau}_e^r$  requested by the VCU and the inverter state transitions are sent to the TI inverter over Controller Area Network (CAN). The maxon load inverter communicates the measured load torque  $\tilde{\tau}_l^m$  and speed  $\tilde{\omega}^m$  to the controller and receives its new reference speed  $\tilde{\omega}^r$  using the industrial field bus EtherCAT (EC) (EtherCAT Technology group, 2019). Finally, a Simcenter SCADAS Data-Acquisition System (DAQ) is included in the setup to measure the speed  $\tilde{\omega}^m$  and two phase currents  $\tilde{i}_a$  and  $\tilde{i}_b$  (the last current  $\tilde{i}_c$  being computed as  $\tilde{i}_c = -\tilde{i}_a - \tilde{i}_b$ ) of the surrogate PMSM, as well as the current  $\tilde{i}_{dc}$  flowing from the DC-bus to the traction inverter during the execution of the tests. Both this DAQ and the real-time computing unit are configured via Ethernet (ETH) from an operator computer.

## 4 REAL-TIME CONTROL STRUCTURE

The real-time computing unit is responsible for the execution of simulation models and the interfacing between them and with the physical components on the test bench. For this purpose, a real-time co-simulation architecture is set up within the unit, which is functionally divided into a master and several slaves (Figure 8).

The *co-simulation master* orchestrates the execution and data exchange of the different *co-simulation* slaves. The master execution is scheduled by a low jitter real-time timer, firing every *master timestep*  $t_i^M$ . At the beginning of each timestep, the master triggers the execution of the slaves and waits for them to return outputs. Co-simulation correction algorithms are then run on the resulting outputs and the corrected values are propagated to the respective slave inputs. Finally, the master waits for the end of the current timestep unless an overrun occurred (Figure 9).

In the present application, a co-simulation slave exposing a Functional Mock-up Interface (FMI) is used to execute the Amesim model (Blochwitz et al., 2012). Apart from the execution of the simulation models, co-simulation slaves are also responsible for specific functionalities of the controller, such as the handling of physical I/O. Indeed, both CAN and EtherCAT slaves are used to communicate with the traction and load inverter respectively.

In general, the computation rate of the master can differ from the one of the slaves. Indeed, the co-simulation slaves can run their models once or more per master timestep  $t^M$  to ensure a specific *virtual rate*  $\frac{t^M}{n_i^S}$  for the numerical integration, where  $n_i^S$  is the number of *micro-steps* of the  $i$ th slave. Subsequently, their results are returned to the master for synchronisation and exchange (Gomes et al., 2017). Due to the master pacing at a lower rate, the slaves see their inputs updated only once every  $n_i^S$  steps. This could introduce artefacts in the co-simulation and generate non-physical frequency content in the signals. To mitigate this effect, the co-simulation master implements numerical techniques aiming to reconstruct the behaviour of the input signals locally to the slave during isolation. An example of such method is provided in (Stettinger et al., 2014).

Each of the previously mentioned slaves, as well as the master, are executed in separate processes and on different CPU cores of the real-time computing unit to minimise computational time jitter. In fact, the most important requirement for a real-time system is time determinism over the carried-out operations. For this reason, the real-time unit is based on a real-time patched (Real-Time Linux Wiki, 2016) Linux kernel that runs the operating system as a fully preemptive process, hence increasing scheduling and computational time determinism.

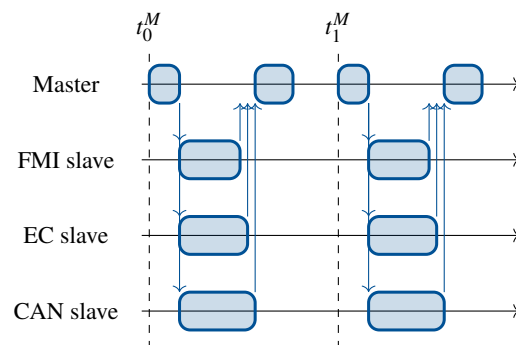


Figure 9: Timing diagram of the real-time controller.

## 5 INTRODUCTION OF SCALING FACTORS

Scaling factors are used to match the full-scale real-time model to the reduced-scale test bench. These coefficients are calculated following the approach used in (Petersheim and Brennan, 2009). The relevant parameters for motor scaling are first identified, based on the torque-speed curve and the limitations of the motor: the maximum motor torque  $\tau^{max}$ , the maximum power  $P^{max}$ , the maximum speed  $\omega^{max}$ , the rotational speed  $\omega$  and the motor torque  $\tau$ . The values of  $\tau^{max}$ ,  $\omega^{max}$  and  $P^{max}$  are listed for the EV motor and for the surrogate PMSM, both with and without considering friction, in Table 2. Three dimensionless variables are then deduced based on the theory of *Applied Dimensional Analysis and Modelling* (Szirtes and Rózsa, 2007):  $\pi_1 = \frac{\omega}{\omega^{max}}$ ,  $\pi_2 = \frac{\tau}{\tau^{max}}$  and  $\pi_3 = \frac{P^{max}}{\omega^{max}\tau^{max}}$ . The detailed calculation of the dimensionless variables can be found in (Joos, 2019).

By using reduced variables  $\pi_1$  and  $\pi_2$ , the torque-versus-speed curves of the EV motor and small PMSMs used on the bench can be plotted along normalised axes, as shown in Figure 10. However, the shapes of the curves do not match: the curve of the EV motor consists of a hyperbolic curve in the flux weakening zone, i.e. where the maximum power is the main limitation of the machine. On the contrary, the ideal torque-versus-speed curve of the PMSM of the test bench presents a wide linear part, as the maximum continuous power is only reached close to the maximum speed. A better match of both curves could be obtained by performing flux weakening on the test bench motor, but falls out of the scope of this paper, as safety margins must be defined to avoid demagnetization of the permanent magnets. Furthermore, considering the non-negligible friction torque on that machine, its corrected curve shows a maximum shaft torque decreasing with speed as the friction torque increases.

Considering the curves in Figure 10, a small area (at low speed and high torque) can be observed where the curve of the surrogate PMSM with friction is located below the one of the EV motor. Therefore, those operating points of the EV motor correspond to an overload of the test bench PMSM. However, when plotting the scaled working points corresponding to the NEDC and WLTC, no point falls in that region and an important margin can even be seen. Therefore, these scaling factors ensure a safe operation of the bench for testing such driving cycles.

By equalling the dimensionless variables for both machines, the scaling factors for torque and speed can be easily computed as the ratios between maximum

torques  $\frac{\tau^{max}}{\tau^{max}}$  and speeds  $\frac{\omega^{max}}{\omega^{max}}$  of both machines. For sake of simplicity, the scaling factors are chosen for the XiL tests without considering friction in Table 2, i.e.  $\frac{\tau^{max}}{\tau^{max}} = 1.03 \times 10^{-3}$  and  $\frac{\omega^{max}}{\omega^{max}} = 0.517$ .

## 6 XiL TEST RESULTS

Closed-loop XiL tests are performed to validate this scalable testing approach. Detailed results on the first part of the NEDC (0 s to 30 s) are first discussed before showing the overall bench performance on the whole cycle. The evolution of speed, currents and torque on the surrogate PMSM are displayed in Figures 11, 12 and 13 respectively.

In Figure 11 the shaft speed  $\tilde{\omega}^m$  of the surrogate SuT measured with the Simcenter SCADAS is compared to the theoretical profile of the NEDC converted in terms of speed of the EV motor.

Figure 11 shows that the speed profile of the NEDC is globally well followed for the small-scale SuT, similarly to the results presented in (Petersheim and Brennan, 2009; Ciceo et al., 2016) for normal-scale benches. Some delays can, however, be reduced through an improved tuning of the driver parameters. The more important delay in the decelerating slope can be linked to the use of different controller parameters for acceleration and braking, as presented in Figure 3. When the reference speed starts decreasing, there is a small delay between the time the acceleration controller stops acting to counter the friction (i.e. the driver releases the throttle) and the time the braking controller starts acting (i.e. the driver starts pressing on the braking pedal). The absence of anti-wind-up loops on these controllers is the most proba-

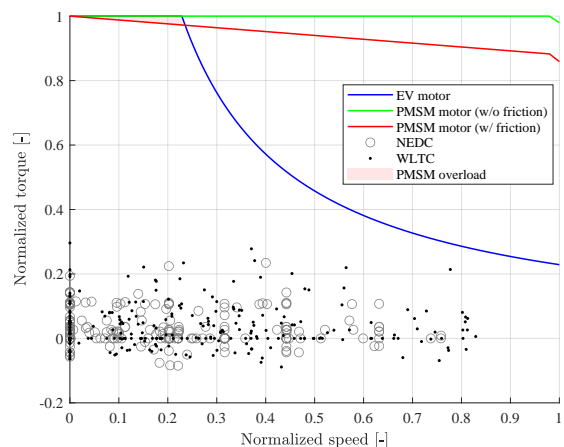
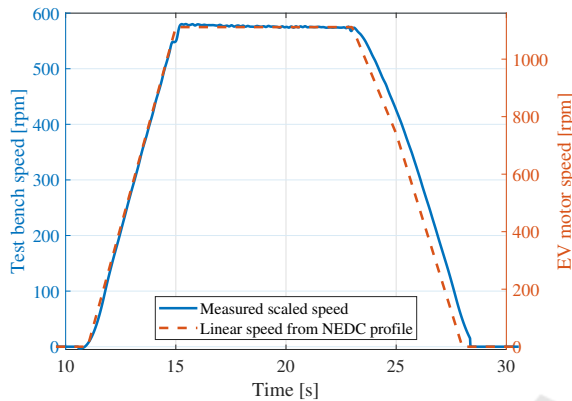


Figure 10: Dimensionless plot of the torque-versus-speed curves of the real and surrogate SuTs, with operating point for two different driving cycles.

Table 2: Maximum ratings of the EV and surrogate SuT motors.

Parameter	Symbol	Value (EV)	Value (PMSM without friction)	Value (PMSM with friction)
Maximum speed	$\omega^{max}$	11.6 krpm	6 krpm	6 krpm
Maximum torque	$\tau^{max}$	270 Nm	279 mNm	263 mNm
Maximum power	$P^{max}$	75 kW	171.7 W	151.2 W


 Figure 11: Speed profile  $\tilde{\omega}^m$  of the surrogate SuT and the first part of the urban cycle of the NEDC.

ble explanation.

Looking in greater detail at Figure 11, a small bump can be observed prior to the plateau speed corresponding to 15 s in the NEDC. It is probably due to the anticipative action of the acceleration controller, monitoring the difference between present and future (0.1 s later) speed set-points. Furthermore, just before the begin of the rising slope at 11 s, a very-low-amplitude negative speed is measured, probably due to some backwards movement of the rotor at the bench start-up. The traction inverter does not seem to be responsible for this, as the phase currents in Figure 12 only show noise before 11 s.

Figure 12 presents the measured currents  $\tilde{i}_a$ , and

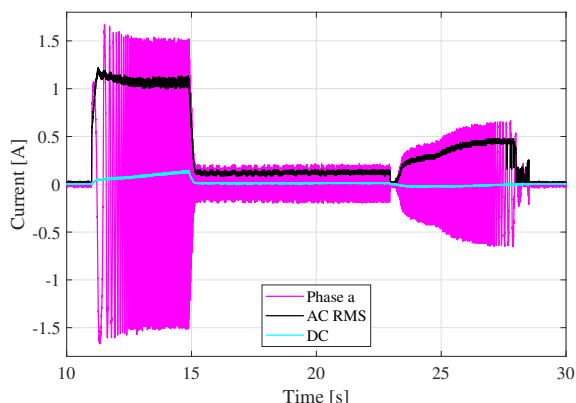


Figure 12: DC-bus, phase and estimated RMS currents in the surrogate SuT during the first part of the urban cycle of the NEDC.

$\tilde{i}_{dc}$  on the SuT. These signals are displayed after having been filtered with a zero-phase second-order Butterworth filter with a 2 kHz cut-off frequency. This filtering is required to match the hypothesis of sinusoidal and balanced phase currents needed to estimate the value of the AC RMS current (also displayed in Figure 12) with the following formula:

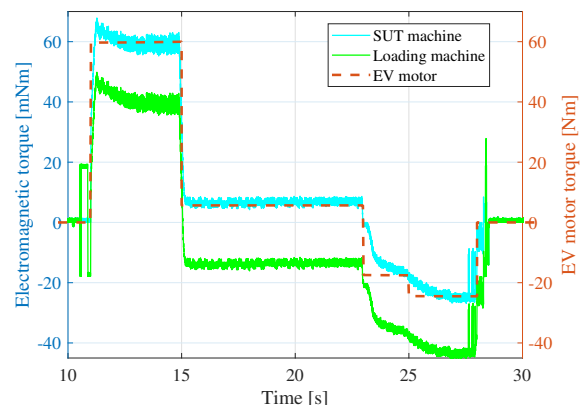
$$\tilde{i}_{rms}^e = \sqrt{\frac{1}{3} (\tilde{i}_a^2 + \tilde{i}_b^2 + \tilde{i}_c^2)}, \quad (6)$$

where the e superscript reflects the estimated nature of this quantity. It is then used together with the torque constant of the machine  $K_t$  to estimate the torque of the surrogate motor  $\tilde{\tau}_e^e$ :

$$\tilde{\tau}_e^e = K_t \sqrt{2} \tilde{i}_{rms}^e \cdot \text{sign}(\tilde{i}_{dc,filtered}), \quad (7)$$

where  $\tilde{i}_{dc,filtered}$  represents  $\tilde{i}_{dc}$  after applying a second-order Butterworth filter with a 5.12 Hz cut-off frequency to prevent noise from affecting the estimated torque direction.  $\tilde{\tau}_e^e$  is an estimate of  $\tilde{\tau}_e^m$ .

The electromagnetic torque  $\tilde{\tau}_e^e$  of the traction PMSM of the bench, estimated from (7), is compared in Figure 13 with the theoretical torque profile to be applied to the EV motor to follow the NEDC (considering a constant 57 % ratio of the braking torque is supplied via the EV motor). An estimate of the loading-machine torque  $\tilde{\tau}_l^e$  using the measurements acquired with the Simcenter SCADAS is also displayed in the figure. This value is computed from  $\tilde{\tau}_e^e$  using (5).


 Figure 13: Torques of the surrogate SuT  $\tilde{\tau}_e^e$  and loading machine  $\tilde{\tau}_l^e$  (left scale), as well as the corresponding torque for the real vehicle (right scale).

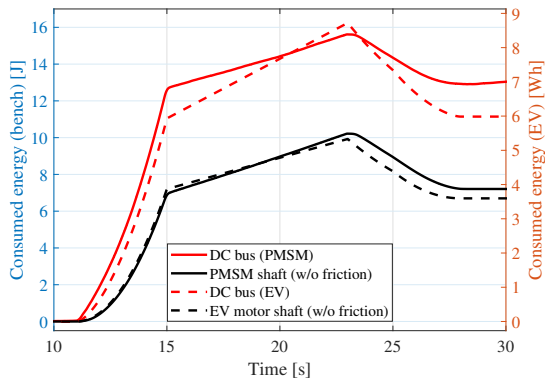


Figure 14: Consumed energy by the surrogate SuT and the corresponding energy requirement from the EV.

The resulting torque profile is globally well followed with the expected scaling factor. However, some delay is observed due to the driver’s dynamic, as already shown for the speed profile in Figure 11. The evolution of  $\tau_f^e$  shows the important part of the friction, which is compensated for by feed-forwarding the estimated friction torque  $\tilde{\tau}_f$  in the real-time simulation model.

Some torque oscillations can be noticed at the beginning and the end of the test. This corresponds to moments where the motors start or stop their rotation. The ones of  $\tau_f^e$  before the acceleration ramp are probably nonphysical and linked to the small backwards movement of the rotor and the way this torque is estimated. However, the later oscillations in the SuT and loading machine torques could have a three-fold origin. Firstly, the sensorless torque control of the TI drive, which uses a speed estimator instead of a sensor, tends to work badly at lower speeds. Indeed, the estimated direction of rotation can be inaccurate when its speed is around 0 rpm. Secondly, the loading machine is controlled in block commutation by the maxon drive, which leads to a jerky torque generation at lower speeds. Finally, the friction torque compensation provided in (5) also shows a disconti-

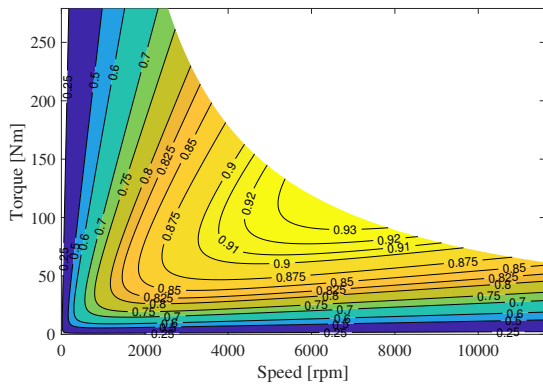


Figure 15: Estimated efficiency map of the EV motor.

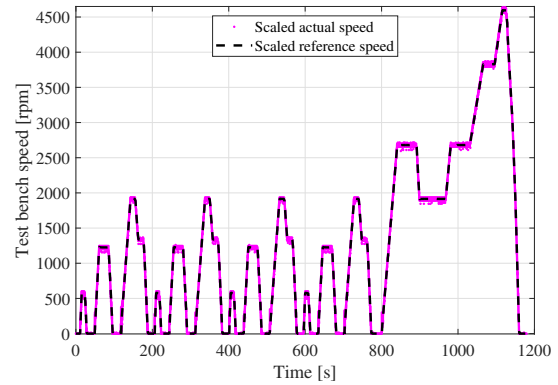


Figure 16: Actual  $\tilde{\omega}^m$  and reference speeds of the surrogate SuT for the full NEDC.

nuity around 0 rpm, which could result in jumps in  $\tau_e^m$  that propagate across the real-time simulation model.

Figure 14 shows the amount of energy absorbed by the traction inverter and delivered to the shaft of the surrogate PMSM excluding friction. For comparison, their theoretical counterparts computed directly from the NEDC speed profile for the EV motor are displayed as well, considering the assumptions made in (Joos, 2019) regarding the EV motor and converter efficiencies. While a constant 95 % converter efficiency is assumed, the efficiency map of the EV motor is computed by adding a 15 % constant offset to the one of the surrogate PMSM, leading to the map displayed in Figure 15.

It appears that the consumed energies at the shaft match relatively well, even if an increased difference can be seen during the decelerating ramp, due to the delay between the measured speed and the theoretical one. However, the energies taken from the DC-bus or battery differ, due to the different motor efficiencies.

The scaled reference and actual speeds of the loading PMSM extracted from the Amesim model over the whole NEDC are shown in Figure 16. They show

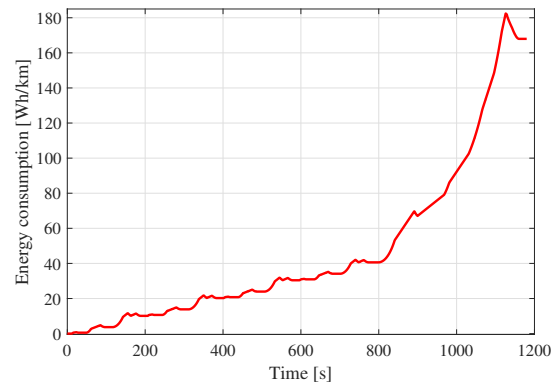


Figure 17: Estimated energy consumed at battery terminals for the real vehicle over the NEDC based on torque and speed measurements on the surrogate SuT.



a good tracking of the reference speed by the maxon drive, as the NEDC profile is easily recognisable.

Finally, the estimated consumed energy per kilometer at the EV battery terminals is displayed in Figure 17 (considering the same assumptions as for Figure 14). The final value of this plot (168 Wh/km) is 17.5 % higher than the claimed consumption of the modelled EV, i.e. 143 Wh/km (BMW, 2017). Such an overestimation can be expected, since the raw estimation of the motor and converter efficiencies are very probably underestimations.

## 7 CONCLUSIONS

In this work, the MBST methodology has been successfully applied to a downscaled XiL test setup used for the validation of EV powertrains, thanks to adequate scaling factors. Validation has been performed on the NEDC. The results also show the influence of the control strategy on the tracking of the speed profile and suggests a possible future use of the small-scale bench for control optimisation.

In future work, the authors will build on this work to increase the power level of the SuT and show the scalability of the proposed framework to real EV components. Additionally, the didactic side of this downscaled setup will be further exploited by further extending its instrumentation. The present PMSM used in SuT will also be exchanged with an induction motor of similar power to enable testing this type of traction motors.

## ACKNOWLEDGEMENTS

This project was partially funded by the European Union's Horizon 2020 research and innovation program under grant agreement No 769506.



The content of this publication does not reflect the official opinion of the European Union. Responsibility for the information and views expressed therein lies entirely with the authors.

## REFERENCES

Blochwitz, T., Otter, M., Åkesson, J., Arnold, M., Clauß, C., Elmqvist, H., Friedrich, M., Junghanns, A.,

Mauss, J., Neumerkel, D., Olsson, H., and Viel, A. (2012). Functional mockup interface 2.0: The standard for tool independent exchange of simulation models. In *Proceedings of the 9th International Modica Conference*.

BMW (2017). Specifications. the new bmw i3. In *BMW media information*, pages 1–8.

Ciceo, S., Mollet, Y., Sarrazin, M., Van der Auweraer, H., and Martis, C. (2016). Model-based design and testing for electric vehicle energy consumption analysis. *Electrotehnică, Electronică, Automatică*, 64:46–51.

EtherCAT Technology group (2019). EtherCAT. [www.ethercat.org](http://www.ethercat.org). Accessed: 2019-08-05.

Fathy, H. K., Filipi, Z. S., Hagena, J., and Stein, J. (2006). Review of hardware-in-the-loop simulation and its prospects in the automotive area. *Proceedings of SPIE - The International Society for Optical Engineering*, 6228.

Fiori, C., Ahn, K., and Rakha, H. A. (2016). Power-based electric vehicle energy consumption model: Model development and validation. *Applied Energy*, 168:257–268.

Gomes, C., Thule, C., Larsen, P. G., and Vangheluwe, H. (2017). Co-simulation: State of the art.

Joos, A. J. (2019). Implementation of a small-scale electrical drive system in Hardware-in-the-Loop simulations. Master's thesis, Brussels Faculty of Engineering.

Obelics consortium (2019). Homepage - Obelics. [obelics.eu](http://obelics.eu). Accessed: 2019-08-05.

Petersheim, M. D. and Brennan, S. (2009). Scaling of hybrid-electric vehicle powertrain components for hardware-in-the-loop simulation. *Mechatronics*, 19:1078–1090.

Popp, A., Sarrazin, M., Van der Auweraer, H., Fodorean, D., Birte, O., Karoly, B., and Martis, C. (2015). Real-time co-simulation platform for electromechanical vehicle applications. *2015 9th International Symposium on Advanced Topics in Electrical Engineering*, pages 240–243.

Real-Time Linux Wiki (2016). Real-Time Linux Wiki. [rt.wiki.kernel.org/index.php/Main\\_Page](http://rt.wiki.kernel.org/index.php/Main_Page). Accessed: 2020-04-01.

Siemens Digital Industries Software (2019). Model-based system testing: Efficiently combining test and simulation for model-based development. [https://www.plm.automation.siemens.com/media/global/en/Model-based%20system%20testing%20WP\\_tcm27-67978.pdf](https://www.plm.automation.siemens.com/media/global/en/Model-based%20system%20testing%20WP_tcm27-67978.pdf).

Stettinger, G., Horn, M., Benedikt, M., and Zehetner, J. (2014). Model-based coupling approach for non-iterative real-time co-simulation. In *2014 European Control Conference (ECC)*, pages 2084–2089.

Szirtes, T. and Rózsa, P., editors (2007). *Applied Dimensional Analysis and Modeling*, pages 133 – 161. Butterworth-Heinemann, Burlington, 2nd edition.

Texas Instruments (2017). InstaSPIN-FOC and InstaSPIN-MOTION User's Guide. <http://www.ti.com/lit/ug/spruhj1g/spruhj1g.pdf>. Accessed: 2019-08-05.

Van der Auweraer, H., Sarrazin, M., and Marques dos Santos, F. (2017). Model-based system testing: A new

drive to integrating test and simulation. In *2017 International Conference on Structural Engineering Dynamics*.

- Williamson, S., Lukic, M., and Emadi, A. (2006). Comprehensive drive train efficiency analysis of hybrid electric and fuel cell vehicles based on motor-controller efficiency modeling. *IEEE Transactions on power electronics*, 21(3):730–740.
- Yang, Y.-P., Shih, Y.-C., and Chen, J.-M. (2014). Real-time driving strategy for a pure electric vehicle with multiple traction motors by particle swarm optimization. *7th IET International Conference on Power Electronics, Machines and Drives (PEMD 2014)*.
- Yang, Z., Shang, F., Brown, I. P., and Krishnamurthy, M. (2015). Comparative study of interior permanent magnet, induction, and switched reluctance motor drives for ev and hev applications. *IEEE Transactions on Transportation Electrification*, 1(3):245–254.

## ACRONYMS

- CAN** Controller Area Network.
- DAQ** Data-Acquisition System.
- EC** EtherCAT.
- ETH** Ethernet.
- EV** Electric Vehicle.
- FMI** Functional Mock-up Interface.
- MBST** Model-Based System Testing.
- NEDC** New European Driving Cycle.
- PI** Proportional Integral.
- PMSM** Permanent-Magnet Synchronous Machine.
- PSU** Power Supply Unit.
- SuT** System-under-Test.
- TI** Texas Instruments.
- VCU** Vehicle Control Unit.
- WLTC** World harmonised Light vehicles Test Cycle.
- XiL** X-in-the-Loop.

## SYMBOLS

- $C_x$  Air penetration coefficient.
- $F_r$  Longitudinal resistive force.
- $J_w$  Wheel inertia.
- $M$  Vehicle mass.
- $R_w$  Wheel radius.
- $S$  Vehicle active area.
- $\dot{x}^r$  Reference longitudinal vehicle speed.

- $\dot{x}$  Longitudinal vehicle speed.
- $\omega^m$  Measured EV motor rotational speed.
- $\omega^r$  Reference EV motor rotational speed.
- $\rho_{\text{air}}$  Air density.
- $\tau^r$  User torque request.
- $\tau_b^{\text{max}}$  Maximum vehicle braking torque.
- $\tau_e^{\text{max}}$  Maximum EV motor torque.
- $\tau_e^{\text{min}}$  Minimum EV motor torque.
- $\tau_b$  Mechanical braking torque.
- $\tau_e^m$  Measured EV motor torque.
- $\tau_e^r$  Reference EV motor torque.
- $\tilde{\omega}^m$  Measured SuT rotational speed on the test bench.
- $\tilde{\omega}^r$  Reference SuT rotational speed on the test bench.
- $\tilde{\tau}_e^m$  Torque at the SuT shaft on the test bench.
- $\tilde{\tau}_e^e$  Estimated SuT torque on the test bench, based on Simcenter SCADAS measurements.
- $\tilde{\tau}_e^r$  Reference SuT torque on the test bench.
- $\tilde{\tau}_f$  Test bench mechanical friction torque.
- $\tilde{\tau}_l^e$  Estimated load motor torque on the test bench, based on Simcenter SCADAS measurements.
- $\tilde{\tau}_l^m$  Measured load motor torque on the test bench.
- $\tilde{i}_{\text{rms}}^e$  Estimated RMS current in the phases of the SuT.
- $\tilde{i}_a$  Current in the phase  $a$  of the SuT.
- $\tilde{i}_b$  Current in the phase  $b$  of the SuT.
- $\tilde{i}_c$  Current in the phase  $c$  of the SuT.
- $\tilde{i}_{dc}$  Current in the DC-bus of the SuT.
- $g$  Constant of gravity.
- $r$  Gearbox ratio.
- $u_b$  Brake command.
- $u_t$  Throttle command.
- $x$  Vehicle longitudinal position.